

THERMO-SOLUTAL STRATIFICATION AND CHEMICAL REACTION EFFECTS ON RADIATIVE MAGNETIZED NANOFLUID FLOW ALONG AN EXPONENTIALLY STRETCHING SENSOR PLATE: COMPUTATIONAL ANALYSIS**MD. Shamshuddin ^{1*}, Faisal Shahzad ², Wasim Jamshed ², O. Anwar Bég³, Mohamed R. Eid ^{4,5} and Tasveer A. Bég⁶**¹*Department of Mathematics, School of Sciences, SR university, Warangal-506371, Telangana, India.**Email: shammaths@gmail.com/md.shamshuddin@sru.edu.in*²*Department of Mathematics, Capital University of Science and Technology (CUST), Islamabad, 44000, Pakistan.**Emails: faisalshahzad309@yahoo.com; wasiktk@hotmail.com*³*Professor of Engineering Science & Director- Multi-Physical Engineering Sciences Group, Mechanical Engineering Department, Corrosion and Coatings Lab, Room 3-08, SEE Building, University of Salford, Manchester, M54WT, UK.**Email: O.A.Beg@salford.ac.uk*⁴*Department of Mathematics, Faculty of Science, New Valley University, Al-Kharga, Al-Wadi Al-Gadid, 72511, Egypt.*⁵*Department of Mathematics, Faculty of Science, Northern Border University, Arar, 1321, Saudi Arabia.**Email: m_r_eid@yahoo.com*⁶*Director- Engineering Mechanics Research, Israfil House, Dickenson Rd., Manchester, M13, UK.**Email: tasveerabeg@gmail.com***Corresponding Author Email: shammaths@gmail.com**Orchid Number: 0000-0002-2453-8492***Abstract**

Motivated by emerging technologies in nanofluid electromagnetic sensor systems, a mathematical model is developed for free convective chemically reacting magnetized Buongiorno nanofluid flow along a stretching exponential Riga plate with dual (thermal and solutal) stratification. Additionally, the effects of radiative heat flux and thermal sink/generation are included. The non-dimensional boundary layer conservation equations are solved with the associated boundary constraints using the Keller Box finite difference scheme, and authentication with earlier studies is conducted. With increasing magnetization parameter, velocity is elevated whereas temperature is suppressed. Increasing Grashof number enhances velocity strongly near the sensor surface region but reduces it further towards the free stream.

The heat transfer is depleted throughout the boundary layer regime with greater Grashof numbers. The thermal distribution is substantially boosted with increment in radiative flux, heat source, thermophoresis and Brownian motion parameters, whereas it is strongly decreased with increment in Prandtl numbers and thermal stratification. The nanoparticle concentration is markedly reduced with rising nanoparticle solutal stratification, Brownian motion parameter, reacting species term and Schmidt number. However, there is a considerable increment in nanoparticle concentration with high thermophoresis values. An increase magnetization parameter also elevates the drag force and wall heat transfer rate whereas it reduces the species gradient at the wall. With increasing chemical reaction, a weak rise in the wall friction and temperature gradient is noticed, but a significant rise is computed in Sherwood number.

Keywords: *Magnetized nanofluid; Buongiorno model; Stretching Riga plate sensor; Thermal radiation; Dual stratification; Heat source/sink; chemical reaction; Numerical.*

1. Introduction

Magnetic nanofluids [1, 2] are a special subset of nanofluids which respond to external magnetic fields. These fluids may be unitary (single magnetic nanoparticle in a base fluid) or hybrid (multiple nanoparticle species). As such magnetic nanofluids offer greater advantages since the flow and thermal transport characteristics can be manipulated both by external magnetic field and also via nanoparticle volume fraction. They are being exploited in for example biomedical systems for targeted drug delivery [3] and heat exchanger systems [4]. The development of these and other technologies has also benefited from mathematical and numerical models. These models require the simultaneous consideration of nanofluid properties, heat transfer, viscous flow and magnetohydrodynamics (MHD). Many different computational methods have also been deployed to solve the nonlinear transport equations inherent to such models. Hamzah *et al.* [5] used a finite element Galerkin technique to compute the heat distribution conjugate of a revolving pipe absorbed in Fe_3O_4 -water nanofluid under transverse magnetic field. A suppressed Nusselt number is observed with greater magnetic field, meanwhile it is enhanced with greater nanoparticle volume fraction, and thermal conductivity ratio. Shafqat *et al.* [6] utilized a space finite element procedure coupled with time Crank-Nicolson to simulate the unsteady magnetohydrodynamic flow of hybrid Al_2O_3 -Cu-water nanomaterial in a saturated cavity open flat channel of an impediment square adiabatic. Dogonchi *et al.* [7] engaged a control volume finite element technique to analyse the effects of nanoparticle shapes hydromagnetic free convective of CuO-water nanofluid in an enclosed complex shape. They showed that shaped-platelet nanoparticles achieve an optima heat

propagation, and an average and local thermal conduction rates are boosted with large Rayleigh number and smaller magnetic field (Hartmann number). Alwawi *et al.* [8] used the finite difference of Keller box technique and Tiwari-Das nanofluid model to simulate the MHD free convection viscoplastic boundary layer flow of Sodium Alginate nanomaterial over a prescribed solid sphere plate temperature. They also considered Graphite oxide (GO), Silver (Ag) and Titanium dioxide (TiO_2) nanoparticles, noting that the latter achieves the greatest local wall drag and local heat gradient magnitudes. Bhatti *et al.* [9] used the perturbation technique and Tiwari-Das nanofluid model to simulate hybrid nanofluid flow under magnetic field effect. They hybridized the mixture of Tantalum and Gold nanoparticles. Additional investigations on magnetized nanomaterials can be obtained from Ahmed *et al.* [10] who addressed carbon nanotube (CNT) performance in transient variable-viscosity nanofluid flow for a shrinking permeable wall. Hasan *et al.* [11] addressed particle shape effects on ferrofluids under low oscillating magnetic field. Sheikholeslami *et al.* [12] adopted a two-phase model to examine the thermal radiation effect on MHD flow.

In recent years, magnetic nanoparticles have infiltrated into electromagnetic sensors wherein they offer improved performance for lower detection limits. They also enable better biosensing designs [13] as a result of their high magnetic properties which are absent in conventional biosystems. Magnetic nanoparticles also permit significant fine tuning for specific point of care applications since the composition, size and magnetic properties can be more precisely modulated. This permits a substantial step up in quality of monitoring and measurement of delicate processes [14]. A particularly attractive sensor for emerging nano-medical applications is the *Riga plate* [15] which features a parallel wall magnetic body force and is constructed with a series of enduring magnets in series with aligned spanwise alternating electrodes. The electromagnetic force is parallel to the Riga sensor plate and decays perpendicularly to the exponential surface. Although, originally developed as an electromagnetic actuator for naval engineering flow control, the presence of magnetic and electric crossed fields that produces the parallel wall electromagnetic force has many possible applications in medicine, coating diagnostics etc. Boundary layer flow characteristics can be successfully altered with modification in the applied electrical and magnetic field strengths on Riga plate sensors. Furthermore, different working fluids can be deployed and thermo-solutal (heat and mass transfer) phenomena can also be incorporated. This has motivated many researchers to explore the performance of Riga and other plate sensor flows with a variety of multi-physics effects. Interesting studies include Salahuddin *et al.* [16] who adopted a Fehlberg Runge–Kutta

procedure to examine the squeezing hydromagnetic flowing non-Newtonian material over a micro-cantilevered sensor plate surface. Shafiq *et al.* [17] utilized an optimal homotopy analysis technique to examine the stagnation point stream of a short memory magneto-viscoelastic fluid along a Riga plate. Several investigators have also explored the performance of magnetic nanofluids in Riga plate systems. Ahmad *et al.* [18] employed a shooting computational scheme and perturbation approach on two-components Buongiorno's nanoscale formulation to analyse the boundary layer mixed convective flowing nanofluid past a porous Riga plate. Hayat *et al.* [19] computed the coefficients of temperature gradient and wall friction for squeezing electromagnetic rotating flow of Carbon (Cu)-Water (H₂O) kerosene oil nanomaterial in two stretching Riga plates, noting that horizontal velocity is elevated with greater magnetization parameter. Ayub *et al.* [20] computed the impact of wall slip on the flowing of magnetic nanomaterial along a Riga plate surface with Brownian movement and the thermophoresis. Anjum *et al.* [21] investigated the impact of stratification heat on magnetized viscoelastic flow along a linear stretching Riga plate with thermal sink/source. They demonstrated that with greater magnetization parameter the flow accelerated. Ellahi [22] examined the flow of non-Newtonian nanofluid in a pipe under the influence of MHD and temperature- dependent viscosity. Ellahi *et al.* [23] studied transport in thermally charged MHD bi-phase flow coatings along slippery walls with non-Newtonian nanofluid and Hafnium particles. Ellahi *et al.* [24] provided a hybrid approach to electro-magnetohydrodynamics flow of nanofluid through porous media.

A scrutiny of the scientific literature has shown that thus far the collective effects of heat sink/source [25], reacting species [26-28] and thermal radiation [29-30] in free convective magnetized Buongiorno nanofluid flow through an exponential stretching Riga plate with dual (thermal and solutal) stratification, has not been considered. This is the focus and the innovation of the current investigation. The flux diffusion Rosseland's model is engaged for the thermal radiation propagation and is applicable for optically dense fluids as considered in Riga plate systems. Chemical reaction is of relevance in electromagnetic corrosion control. The controlling momentum, heat transfer and chemical reaction equations with modified Grinberg magnetic body force term are formulated, with associated boundary conditions in a Cartesian coordinate system. Using appropriate similarity transformations, the resulting dimensionless model is solved by the efficient, finite implicit difference Keller Box method. The authentication of the results is done by comparative analysis with aforementioned studies. The impact of magnetization parameter (H), Grashof number (Gr), radiative flux parameter (Rd), heat source parameter, thermophoresis term (Nt), (Q), Brownian movement term (Nb), Prandtl

number (Pr), thermal stratification term (St), nanoparticle solutal stratification parameter (Sm), species reaction term (δ) and Schmidt number on the flow rate, temperature, nanoparticle concentration, skin friction, Nusselt number and Sherwood number is visualized graphically and in tables. The analysis find applications in emerging applications in magnetic nanobiosensors [31] and molecular monitoring sensing systems exploiting magnetic nanoparticles and Riga sensors in biochemical engineering [32].

2. Mathematical Model

The physical description under consideration is shown in **Fig. 1**. Incompressible, natural convective radiative chemically reacting magnetized nanofluid flow through an exponential stretchy Riga electromagnetic plate is investigated. Buongiorno's nanofluid formulation is employed, which features thermophoresis and Brownian movement. The nanofluid is optically dense and thermal flux radiation is simulated with the Rosseland model. A reacting homogenous species of order one is assumed for the reactive nanoparticles. Heat source/sink is also present as are thermal and solutal (mass) stratification effects. The Riga plate sensor is on the direction of x-axis. The magnetization at the plate ($y = 0$) is $M = M_0 x$ with unvarying energy and species at the wall T_w, C_w that are greater than the ambient heat and reacting species T_∞, C_∞ . The stretched rate of the Riga plate in x-axis is $u = U_0 e^{x/L}$, where U_0 denotes a reference velocity. Generalizing the models of Supian *et al.* [33], Yusof *et al.* [34] and Hayat *et al.* [35], the controlling equations for reacting species, velocity, heat transfer and nanoparticle reaction are formulated as follows in an (x, y) coordinate system:

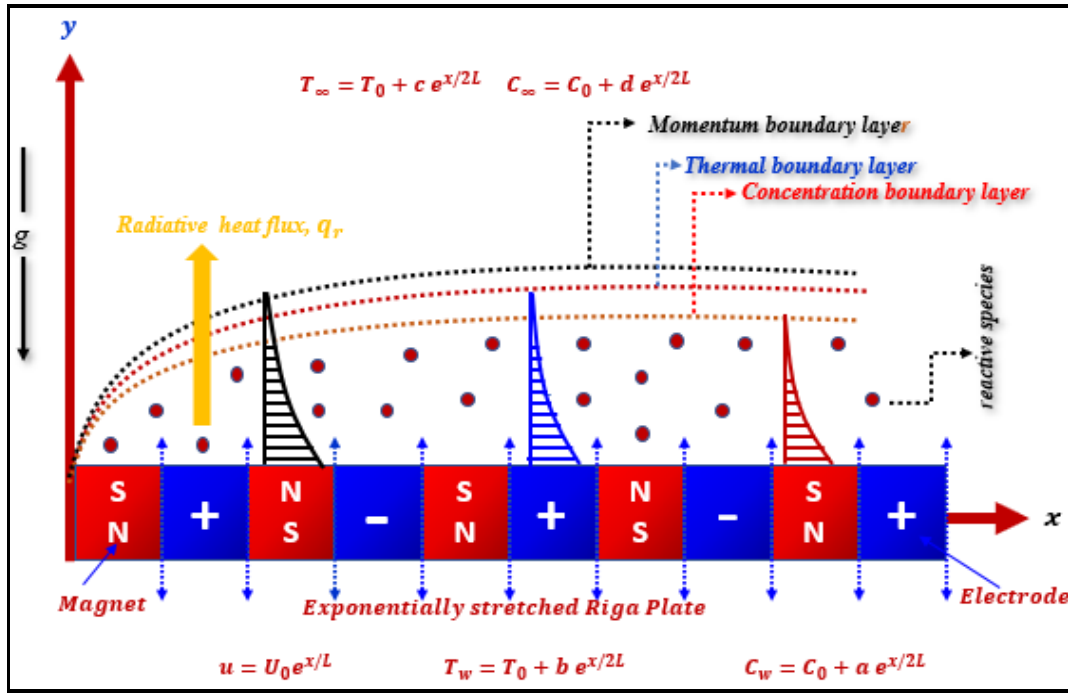


Fig. 1. Physical model for magnetized nanofluid flow along a stretching Riga sensor plate

$$\frac{\partial u}{\partial x} + \frac{\partial v}{\partial y} = 0$$

(1)

$$u \frac{\partial u}{\partial x} + v \frac{\partial u}{\partial y} = \nu \frac{\partial^2 u}{\partial y^2} + g\beta_0(T - T_\infty) + \frac{\pi J_0 M_0}{8\rho} e^{-\frac{\pi}{a_1} y}$$

(2)

$$u \frac{\partial T}{\partial x} + v \frac{\partial T}{\partial y} = \alpha \frac{\partial^2 T}{\partial y^2} - \frac{1}{\rho C_p} \frac{\partial q_r}{\partial y} + \tau \left[D_B \frac{\partial C}{\partial y} \frac{\partial T}{\partial y} + \frac{D_T}{T_\infty} \left(\frac{\partial T}{\partial y} \right)^2 \right] + \frac{Q_0(T - T_\infty)}{\rho C_p},$$

(3)

$$u \frac{\partial C}{\partial x} + v \frac{\partial C}{\partial y} = D_B \frac{\partial^2 C}{\partial y^2} + \frac{D_T}{T_\infty} \left(\frac{\partial^2 T}{\partial y^2} \right) - K_r(C - C_\infty)$$

(4)

$$y=0: \quad u = U_0 e^{x/L}, \quad v = 0, \quad T = T_w = T_0 + b e^{x/2L}, \quad C = C_w = C_0 + a e^{x/2L}$$

$$y \rightarrow \infty: \quad u = 0, \quad v = 0, \quad T = T_\infty = T_0 + c e^{x/2L}, \quad C = C_\infty = C_0 + d e^{x/2L}$$

(5)

In Eqns. (1)-(5) the following notation applies: u and v denote flow rate modules in x , y planes, separately, T is temperature, kinematic viscosity is ν , nanofluid density is ρ , plate permanent magnetization is M_0 , applied electrode current density is j_0 , heat diffusion is α , heat expansivity is β_0 , thermal capacity is C_p , thermal sink/source is Q_0 , nanoparticles molecular diffusivity is D_B . thermophoresis diffusion is D_T , chemical reaction parameter is K_r , unidirectional radiative flux is q_r . The radiation term in the energy equation is obtained utilizing Rosseland's approximation [36]

$$q_r = -\frac{4\sigma^*}{3k^*} \frac{\partial T^4}{\partial y}. \quad (6)$$

Here σ_1 is Stefan-Boltzmann radiative constant, k_1 is absorption coefficient. Taylor expansion of T^4 about T_∞ , and neglecting terms of higher order, gives $T^4 \approx 4T_\infty^3 T - 3T_\infty^4$.

Invoking the following transformations [35]:

$$\eta = \sqrt{\frac{U_0}{2\nu L}} y e^{x/2L}, \quad u = U_0 f'(\eta) e^{x/L}, \quad v = -\sqrt{\frac{\nu U_0}{2L}} e^{x/2L} [\eta f'(\eta) + f(\eta)], \quad (7)$$

$$\theta = \frac{T - T_\infty}{T_w - T_0}, \quad \phi = \frac{C - C_\infty}{C_w - C_0}$$

Substitution of Eqn. (7) in Eqns. (1)-(5), the mass conservation is inevitably gratified, and the reduced flow rate, heat and nanoparticle species equations emerges in the following dimensionless, coupled, nonlinear ordinary differential equations:

$$f''' + f f'' - 2f'^2 + Gr\theta + H e^{-\Delta\eta} = 0 \quad (8)$$

$$(1 + Rd)\theta'' + Pr(f\theta' - f'\theta - St f' + Nb \theta' \phi' + Nt \theta'^2 + Q \theta) = 0 \quad (9)$$

$$\phi'' + Sc f \phi' - Sc f' \phi + \frac{Nt}{Nb} \theta'' - Sc Sm f' - 2Sc \delta \phi = 0 \quad (10)$$

The associated dimensionless boundary constraints for the Riga plate and edge of the boundary layer become:

$$\begin{aligned} f'(0) &= 1, f(0) = 0, \theta(0) = 1 - St, \phi(0) = 1 - Sm \\ f'(\infty) &\rightarrow 0, \theta(\infty) \rightarrow 0, \phi(\infty) \rightarrow 0 \end{aligned} \quad (11)$$

The similarity quantity η is used and the differential order is denoted with prime. The dimensionless terms featured in Eqns. (8-10) are defined as:

$$\begin{aligned} St &= \frac{c}{b}, Sm = \frac{d}{a}, Gr = \frac{2g \beta (T_w - T_0)L}{U_0^2 e^{\frac{2x}{L}}}, \Delta = \frac{-\pi}{a} \sqrt{\frac{2\nu L}{U_0}} e^{\frac{2x}{L}}, H = \frac{\pi J_0 M_0 L}{8\rho U_0^2 e^{\frac{2x}{L}}} \\ Pr &= \frac{\nu}{\alpha}, Rd = \frac{16\sigma^* T_\infty^3}{3k k^*}, Nt = \frac{\tau D_B (T_w - T_0)}{\nu T_\infty}, Nb = \frac{\tau D_B (C_w - C_0)}{\nu}, Sc = \frac{\nu}{D_B}, \\ Q &= \frac{2Q_0 L}{\rho C_p U_0 e^{\frac{2x}{L}}}, \delta = \frac{L K_r}{U_0} \end{aligned} \quad (12)$$

Here S_t, S_m are heat and stratification solutal terms respectively, Gr is thermal Grashof number, Δ denotes non-dimensional Riga term related to the electrode and magnetic width, H stands for body force magnetic modification, Pr is Prandtl number, R is thermal radiative term, Nt, Nb are thermophoresis and Brownian parameters of the Buongiorno model, Sc is

Schmidt number, Q indicates thermal sink/source/ term and δ symbolizes the chemical reaction species term.

Important design quantities are the wall friction factor, Nusselt and mass gradient numbers that may be expressed correspondingly as follows:

$$C_f = \frac{\tau_w|_{y=0}}{\rho u_w^2}, \quad Nu = -\frac{x q_w|_{y=0}}{k(T_w - T_\infty)}, \quad Sh = -\frac{x q_m|_{y=0}}{D_B(C_w - C_\infty)} \quad (13)$$

In Eqn. (13), the dimensional shear stress, thermal flux and solutal flux are described as:

$$\tau_w = \mu \frac{\partial u}{\partial y} \Big|_{y=0}, \quad q_w = -k(1+R) \frac{\partial T}{\partial y} \Big|_{y=0}, \quad q_m = -D_B \frac{\partial C}{\partial y} \Big|_{y=0} \quad (14)$$

Invoking the non-dimensional transformations in Eqn. (12), we get:

$$\begin{aligned} \sqrt{\frac{2L}{x}} \sqrt{Re_x} C_f = f''(0), \quad \sqrt{\frac{2L}{x}} \frac{Nu_x}{\sqrt{Re_x}} = -(1+R) \frac{1}{1-St} \theta'(0), \\ \sqrt{\frac{2L}{x}} \frac{Sh_x}{\sqrt{Re_x}} = -\frac{1}{1-Sm} \phi'(0) \end{aligned} \quad (15)$$

Where $Re_x = U_0 e^{x/L} x / \nu$ indicates local Reynolds number. The local wall friction (skin surface shear stress), local thermal gradient number (plate thermal transport gradient) and local mass gradient number (plate nanoparticle species transport) computed in the numerical solution in the next section are $C_f Re_x^{1/2}$, $Nu_x Re_x^{-1/2}$ and $Sh_x Re_x^{-1/2}$ respectively. These are obtained by simple transposition of Eqn. (15).

3. Numerical Solution with Keller-Box Finite Difference Technique

To have a solution for the nonlinear ordinary differential Eqns. (8)– (10) with associated boundary constraints (11), the second order accurate finite difference Keller box method [37] has been deployed, coded in symbolic software MATLAB. The stages intrinsic to this numerical scheme are summarized in the flow chart in **Fig. 2**. This method is very popular for parabolic differential equation systems such as boundary layer flows and has been employed widely in recent years for magnetized nanofluid flows [38-41].

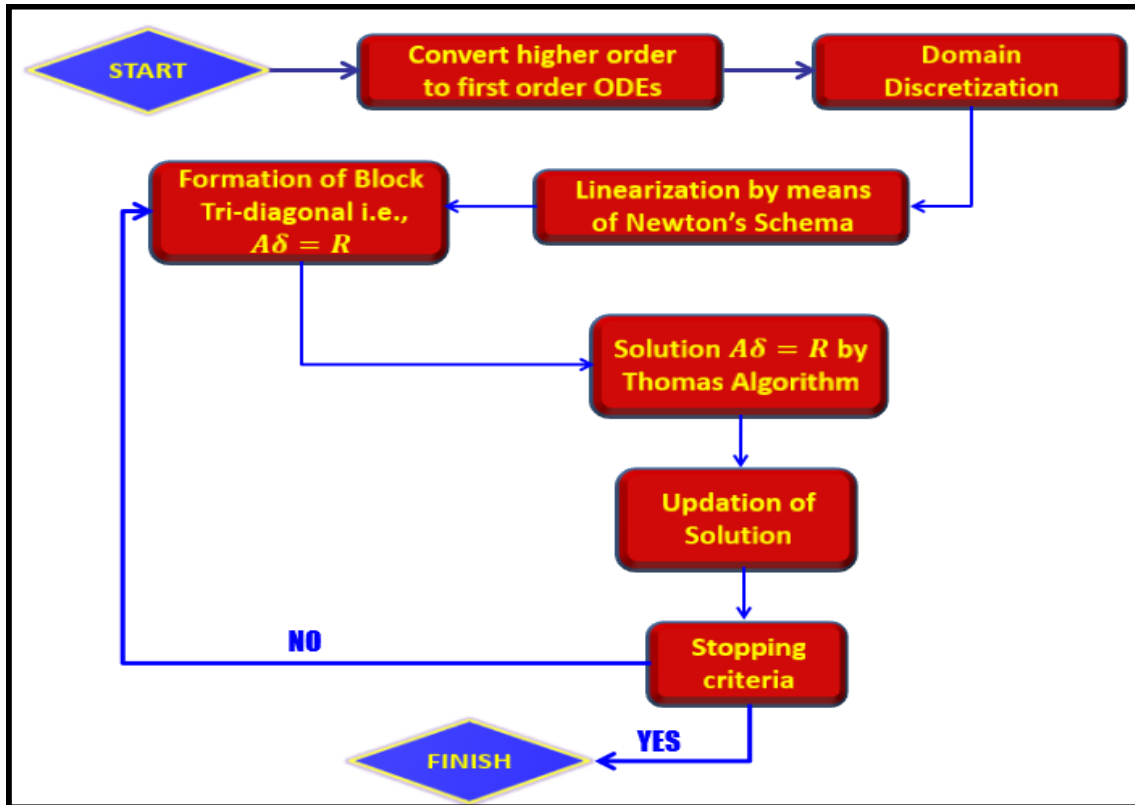


Fig. 2. A diagram of the sequences of the Keller box technique.

The first stage of the Keller box method is the reduction of the multi-order ordinary differential equation system to system of multiple order-one ordinary derivative equations. The substitutions $y_1, y_2, y_3, y_4, y_5, y_6$ and y_7 are demarcated where:

$$y_1 = f, y_2 = f', y_3 = f'', y_4 = \theta, y_5 = \theta', y_6 = \phi, y_7 = \phi'. \quad (16)$$

$$y_1' = y_2, \quad (17)$$

$$y_2' = y_3, \quad (18)$$

$$y_3' = -y_1 y_3 + 2y_2^2 - Gry_4 - He^{-\Delta\eta}, \quad (19)$$

$$y_4' = y_5, \quad (20)$$

$$y_5' = \frac{Pr(y_1 y_5 - y_2 y_4 - St y_2 + Nb y_5 y_7 + Nt y_5^2 + Q y_4)}{(1 + Rd)}, \quad (21)$$

$$y_6' = y_7, \quad (22)$$

$$y_7' = -Sc y_1 y_7 + Sc y_2 y_6 - \frac{Nt}{Nb} y_5' + Sc Sm y_2 + 2Sc \delta y_6, \quad (23)$$

$$\left. \begin{aligned} y_2(0) = 1, y_1(0) = 0, y_4(0) = 1 - St, y_6(0) = 1 - Sm, \\ y_2(\infty) = 0, y_4(\infty) = 0, y_6(\infty) = 0. \end{aligned} \right\} \quad (24)$$

Appropriate finite difference approximations are then introduced, and the consequential algebraic nonlinear system is then linearized and solved with a block elimination matrix technique with the aid of a Thomas algorithm. An appropriate stepping distance in the η -direction is used. Solutions are readily generated for flow velocity (f'), temperature (θ) and

nanoparticle species(ϕ) with carefully selected values of the control terms (Sc, H, Sm etc).

4. Verification of Computed Results

The validity of the Keller box algorithm is verified by comparing the Nusselt number (wall temperature gradient) solutions to the earlier study of Qureshi [42] in the absence of radiative flux ($R = 0$), neglecting nanoscale effects ($Nb = Nt = 0$), negating dual stratification effects ($St = Sm = 0$) and without heat absorption/generation ($Q = 0$). Table 1 shows that very close correlation is obtained confirming the correctness of the Keller box code.

Table 1. Comparing $-\theta'(0)$ with variation in Prandtl number and with $Rd = Nb = Nt = St = Sm = 0, Q = 0$.

Pr	Qureshi [42]	Keller box solution
0.72	0.8087618	0.8087612
1.0	1.0000000	1.0000000
3.0	1.9235742	1.9235734
7.0	3.0731465	3.0731465
10	3.7205542	3.7205511

5. Results and Discussion

Detailed solutions have been computed for the hydrodynamic, thermal and nanoparticle species characteristics for variation in all key parameters. The results for flow rate, heat dispersion and reacting nanoparticle (i. e. $f'(\eta), \theta(\eta)$ and $\phi(\eta)$) with transverse coordinate (η) are visualized in **Figs. 3-17**. In all figures, the following physically appropriate data for Riga plate sensor flows is prescribed (unless otherwise stated) which has been selected from [18]-[21] and [33]-[34]: $H = 0.5, Pr = 7, Rd = 0.1, Q = 0.3, Nb = Nt = 0.2, Sc = 0.3, St = Sm = 0.1, \delta = 0.4$.

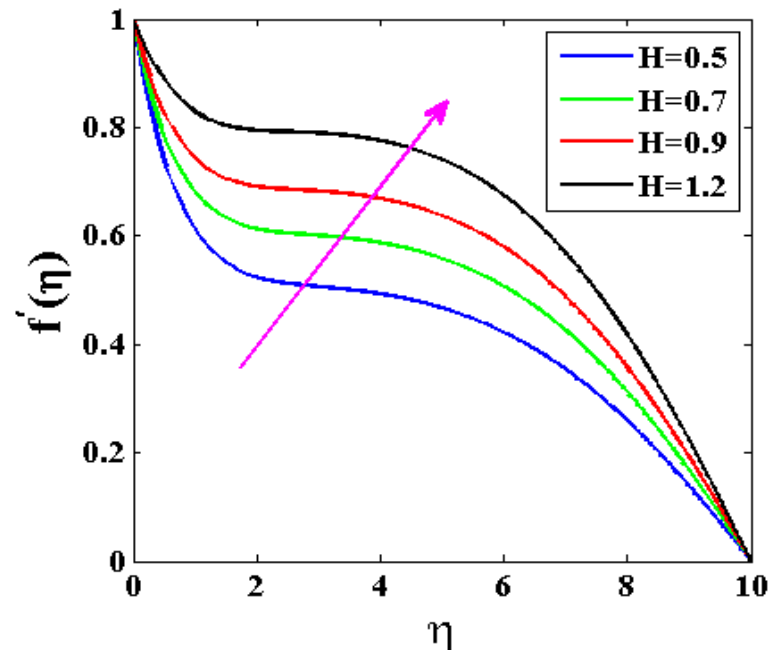


Fig. 3. Velocity ($f'(\eta)$) profiles for various values of H .

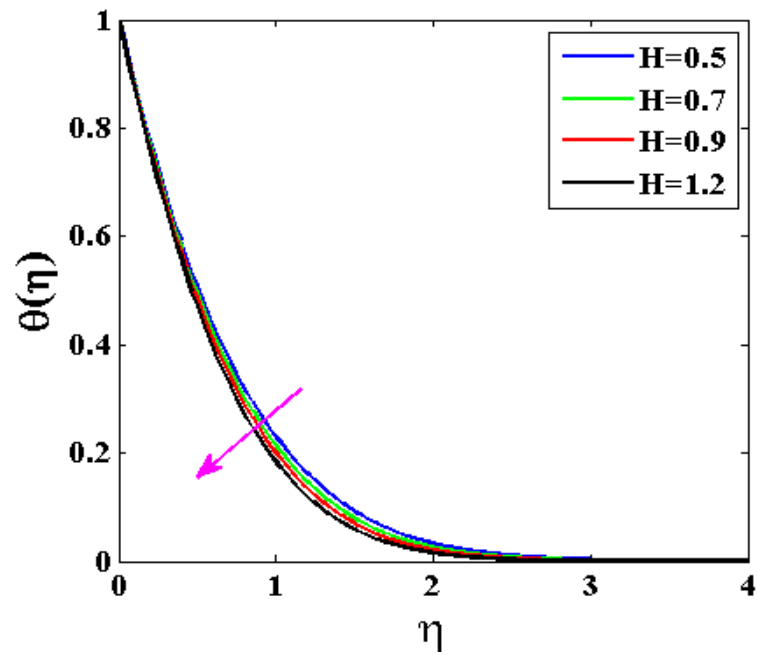


Fig. 4. Temperature ($\theta(\eta)$) profiles for diverse values of H .

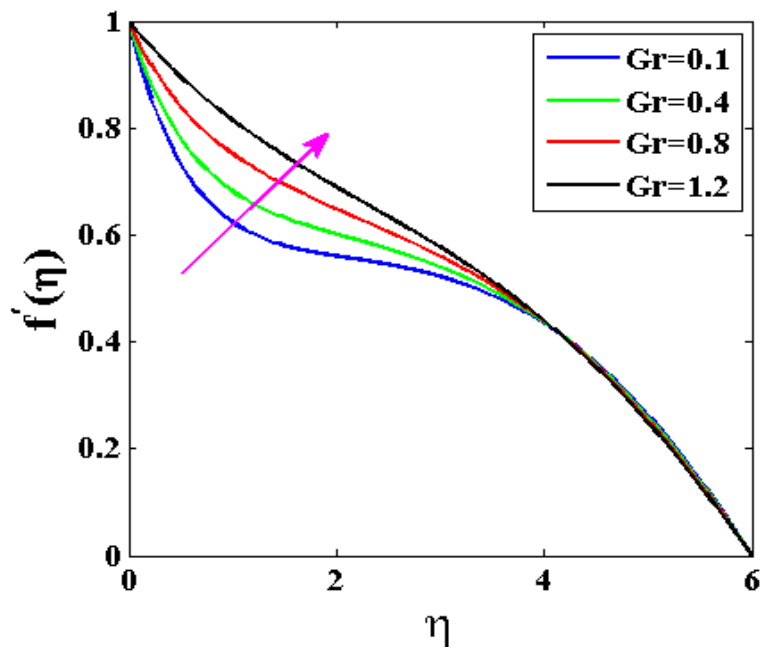


Fig. 5. Velocity ($f'(\eta)$) profiles for various values of Gr .

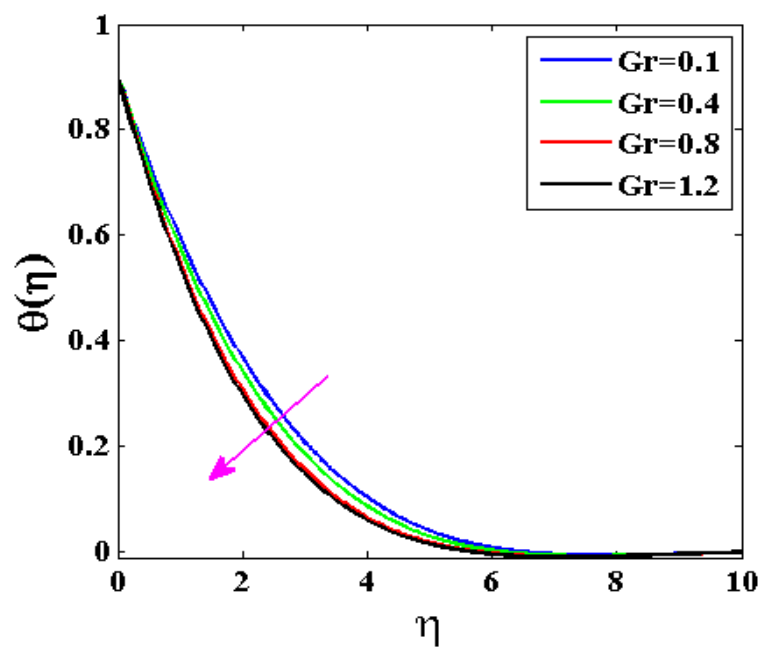


Fig. 6. Heat distribution ($\theta(\eta)$) profiles for diverse values of Gr .

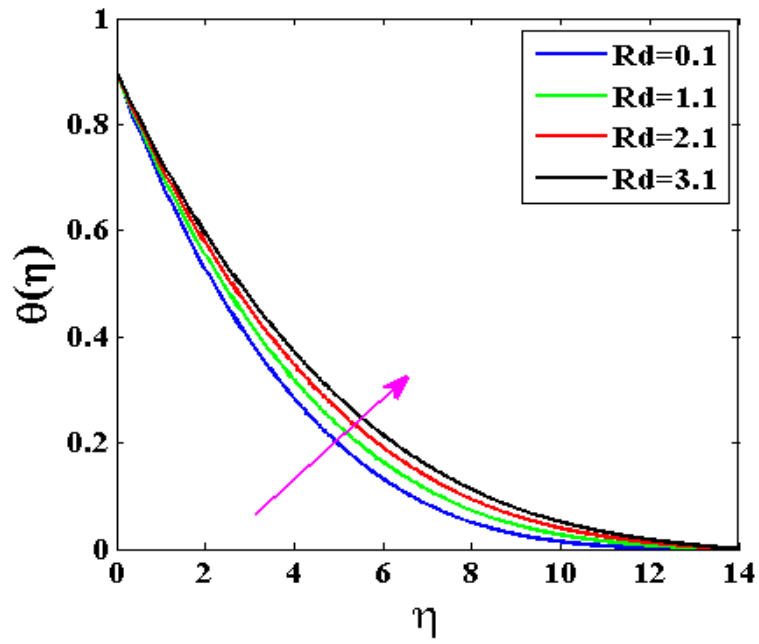


Fig. 7. Temperature ($\theta(\eta)$) profiles for various values of Rd .

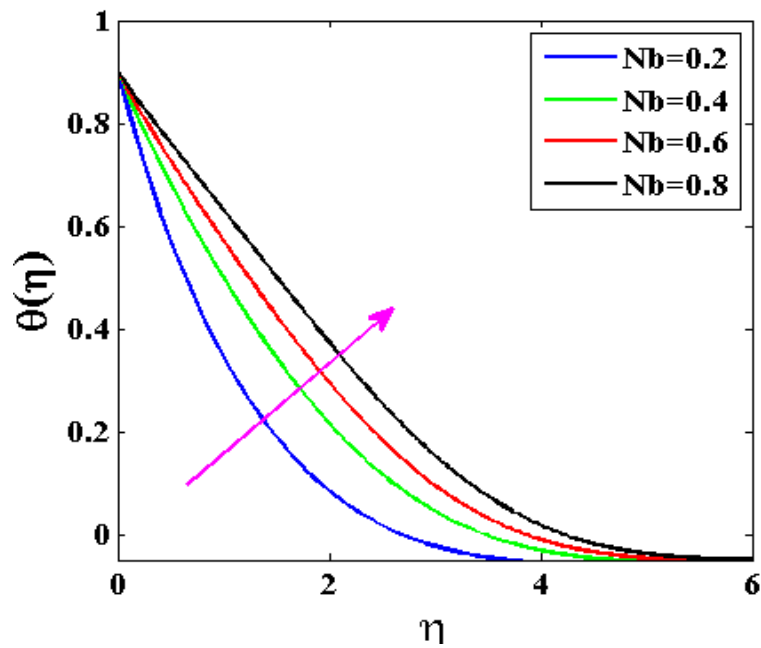


Fig. 8. Heat propagation ($\theta(\eta)$) profiles for various values of Nb .

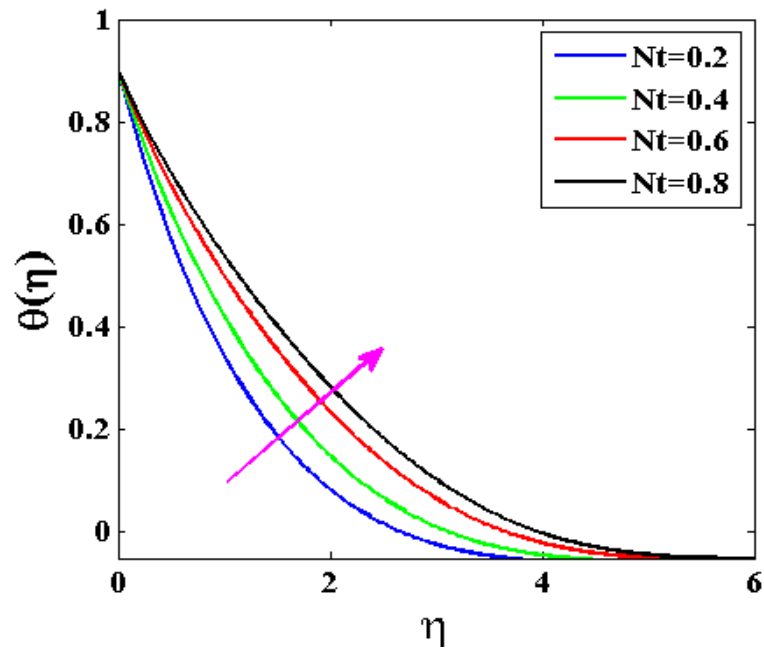


Fig. 9. Temperature ($\theta(\eta)$) profiles for various values of Nt .

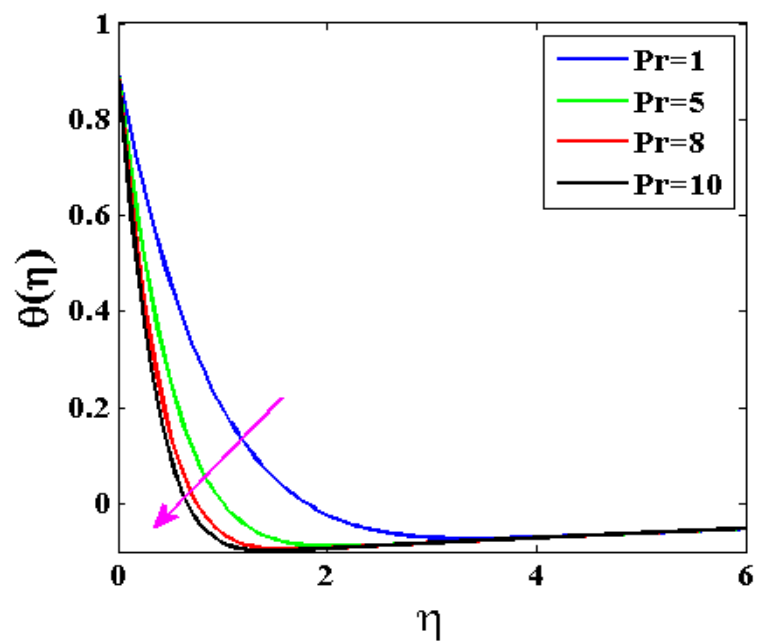


Fig. 10. Temperature ($\theta(\eta)$) profiles for various values of Pr .

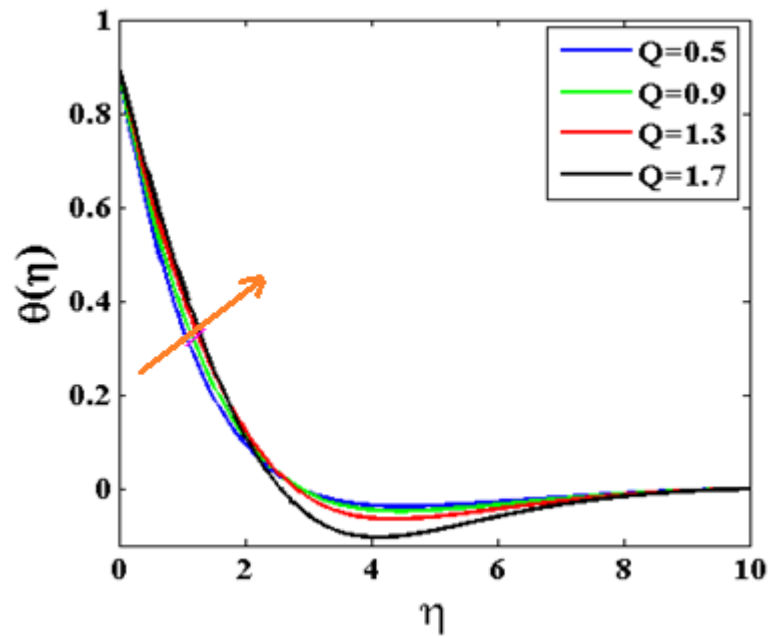


Fig. 11. Temperature ($\theta(\eta)$) profiles for various values of Q .

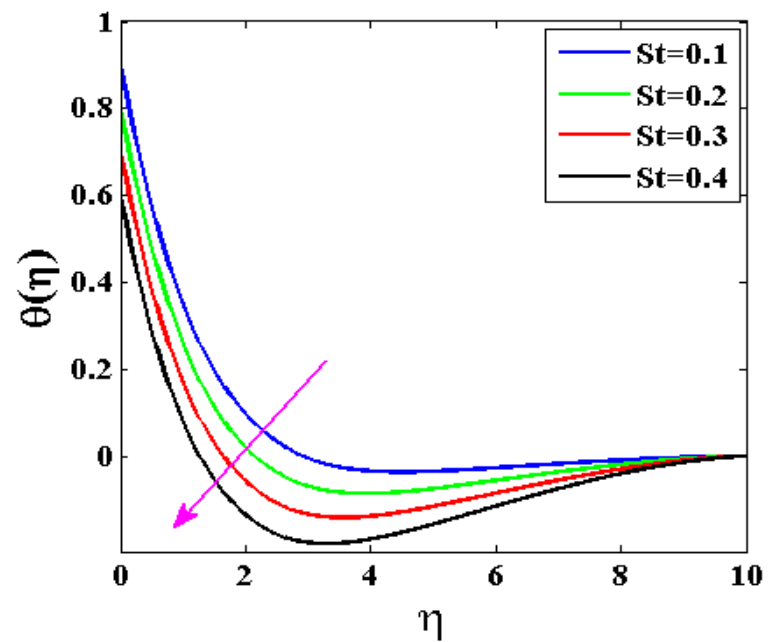


Fig. 12. Temperature ($\theta(\eta)$) profiles for various values of St .

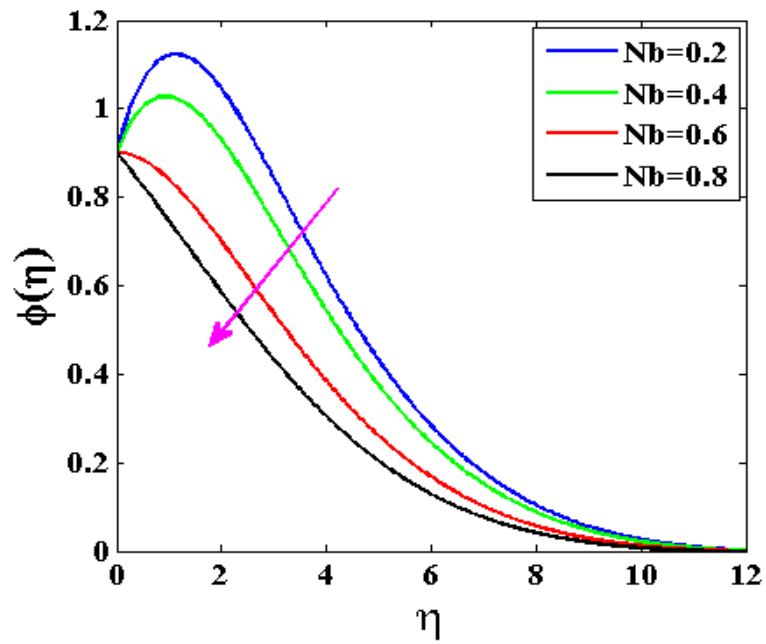


Fig. 13. Nanoparticle concentration ($\phi(\eta)$) profiles for various values of Nb .

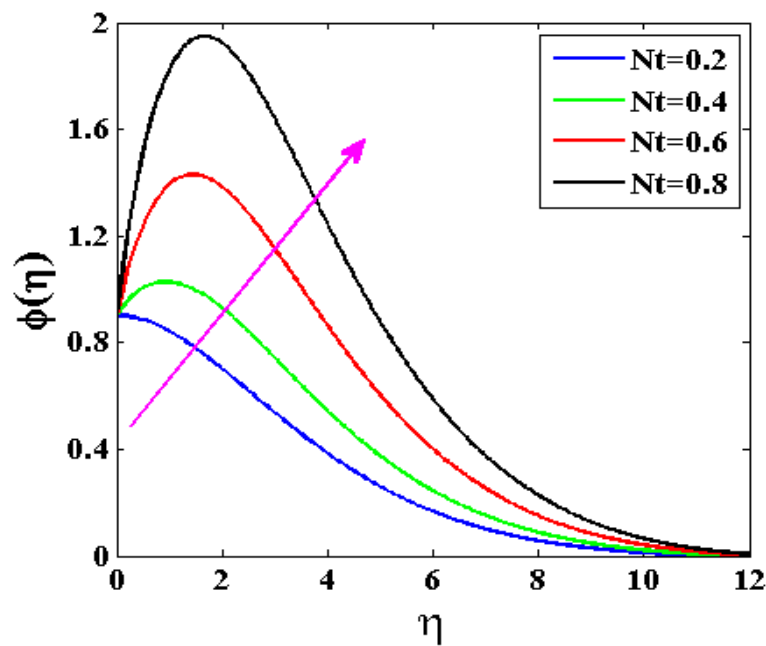


Fig. 14. Nanoparticle concentration ($\phi(\eta)$) profiles for various values of Nt .

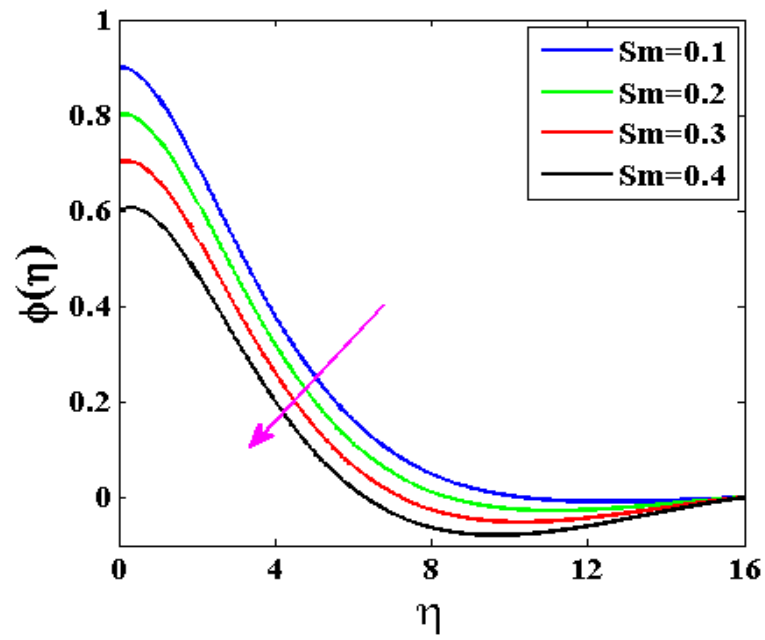


Fig. 15. Nanoparticle concentration ($\phi(\eta)$) profiles for various values of Sm .

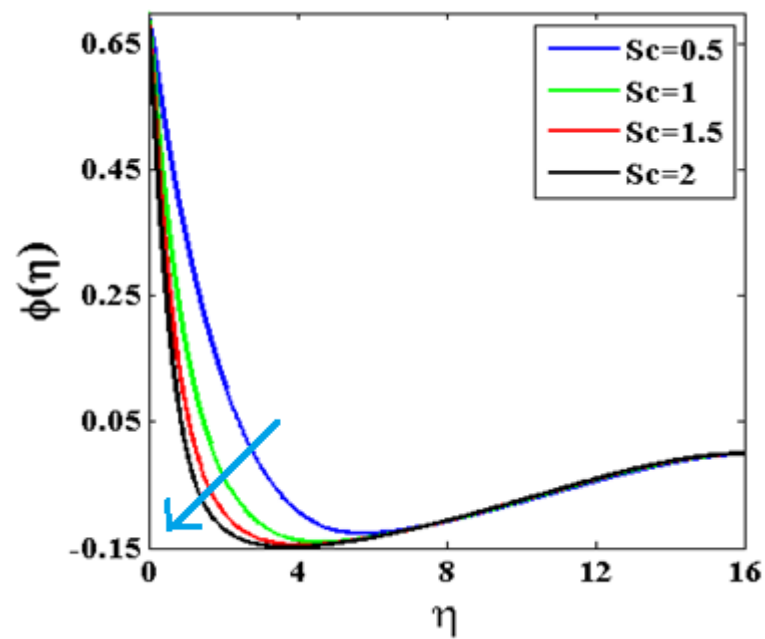


Fig. 16. Nanoparticle concentration ($\phi(\eta)$) profiles for various values of Sc .

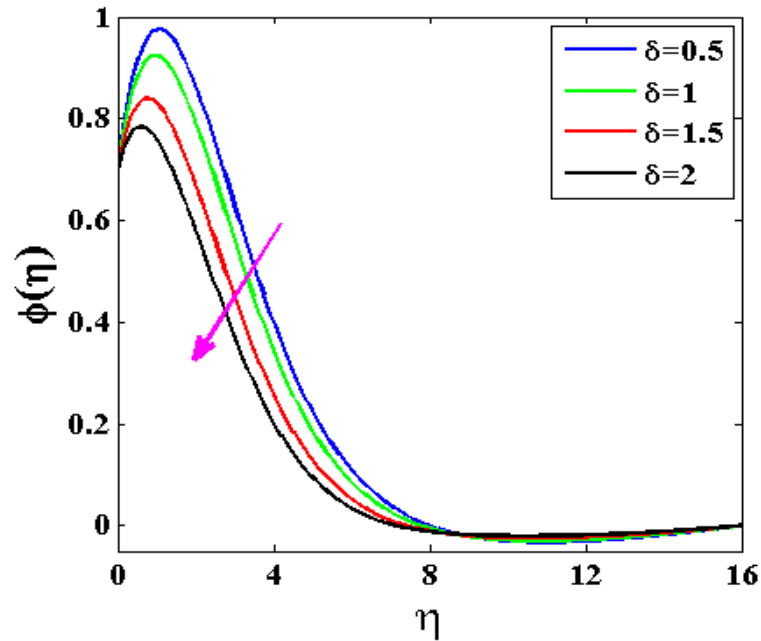


Fig. 17. Nanoparticle concentration ($\phi(\eta)$) profiles for various values of δ .

Table 2: Results of wall friction $C_f Re_x^{1/2}$, thermal gradient $Nu_x Re_x^{-1/2}$ and Sherwood number $Sh_x Re_x^{-1/2}$ at the Riga plate sensor surface (wall)

H	Gr	Rd	Nb	Nt	Pr	Q	Sc	δ	St	Sm	$C_f Re_x^{1/2}$	$Nu_x Re_x^{-1/2}$	$Sh_x Re_x^{-1/2}$
0.5	2	0.1	0.1	0.2	7	0.3	0.3	0.4	0.1	0.1	0.18281	1.48902	0.59603
0.7											0.31953	1.53711	0.57823
0.9											0.44952	1.57755	0.56174
	0.1										0.87102	1.33349	0.63284
	0.4										0.97528	1.35914	0.59724
	0.8										1.10903	1.38927	0.55393
		0.1									0.86738	1.17345	0.20454
		1.1									0.87491	1.52916	1.01403
		2.1									0.87919	1.78985	1.36344
			0.2								0.87130	1.31095	1.95027
			0.4								0.87166	1.28139	2.16979
			0.6								0.87202	1.25237	2.24293
				0.2							0.87120	1.32023	6.43112
				0.4							0.87156	1.29417	3.15221
				0.6							0.87192	1.26874	0.03404
					5.0						0.87213	1.26040	8.24908
					8.0						0.85401	3.16447	5.12117
					10						0.84958	4.07348	3.59389
						0.5					0.87103	1.12873	8.49322
						0.9					0.84212	1.98466	7.43758
						1.3					0.81767	4.50181	5.78605
							0.5				0.87119	1.31680	0.24605

							1.0				0.87124	1.31001	0.87227
							1.5				0.87126	1.30435	1.04600
								0.5			0.87108	1.32820	0.92887
								1.0			0.87111	1.32480	1.13519
								1.5			0.87114	1.32129	1.36670
									0.1		0.87102	1.33349	0.63284
									0.2		0.86316	1.50502	0.60628
									0.3		0.85521	1.72617	0.57902
										0.1	0.87103	1.33260	0.96838
										0.2	0.87103	1.33305	0.82158
										0.3	0.87102	1.33349	0.63284

Figs. 3 and 4 denote the impact of the Riga magnetic term, $H = \frac{\pi J_0 M_0 L}{8\rho U_0^2 e L}$, on velocity and temperature, respectively. With increment in H values, there is a strong accentuation in velocity profiles (Fig. 3) which exhibit a sigmoidal topology. Peak velocity is obtained at the Riga plate and the velocity decays into the free stream. Flow acceleration is therefore generated since the modified body force, $+H e^{-\Delta\eta}$, in the momentum equation is *assistive*, not inhibitive, since it aligned with the sensor (plate surface) and is not transverse to it, as in Lorentzian forces encountered in conventional magnetohydrodynamics [43]. Momentum (hydrodynamic) boundary layer thickness is therefore reduced with high values of magnetization term, H . Temperature as observed in Fig. 4, is conversely suppressed with rising values of H . Since the aligned magnetic body force assists momentum development, the nanofluid does not expend extra work and does not drag against the magnetic field. This induces a cooling effect in the regime and decreases thermal boundary layer thickness.

Figs. 5 and 6 illustrate the influence of the Grashof number Gr , on flow rate and heat dispersion, respectively. Near the sensor surface (wall) a strong acceleration (Fig 5) is generated in the flow and the profiles morph from parabolic to approximately linear decays. However further into the boundary layer there is a weak reduction in velocity sustained to the free stream. , $Gr = \frac{2g \beta(T_w - T_0)L}{U_0^2 e L}$ and represents the ratio of thermal buoyancy force to viscous

force in the boundary layer. For $Gr < 1$ viscous force dominates the thermal buoyancy and vice versa for $Gr > 1$. As Gr is increased the thermal buoyancy term, $+Gr\theta$, in the momentum Eqn (8) is increased which assists the flow and induces a boost in velocities. However the upsurge in thermal buoyancy force generates a strong decrement in temperatures (Fig. 6) which is maintained along the transverse Riga plate boundary. The thickness of the thermal boundary

layer is substantially depleted with huge values of Gr . In all the heat distributions there is a smooth monotonic descent towards the free stream.

Fig 7 displays the impact of radiative parameter (Rd) on temperature distribution. A strong accentuation in temperature is observed for a rising radiation term (Rd) and thermal boundary layer thickness is increased. The magnetic nanofluid is energized with greater values of radiative flux. $Rd = \frac{16\sigma^*T_c^3}{3k k^*}$ signifies the relative involvement of radiative thermal dispersion and thermal conduction heat transfer in the regime. When $Rd > 1$, radiative heat controls the heat conductivity and the converse is the case when $Rd < 1$. For $Rd = 1$ both thermal transport modes contributed correspondingly. When $Rd = 0$, radiative effects vanish. Asymptotically smooth distributions are seen in the free stream confirming that an adequately high infinity boundary constraint is given in the Keller box code. The presence of radiative heat effectively encourages heat transfer in the sensor regime.

Figs. 8 and 9 illustrate the response in temperature to a variation in nanoscale parameters i.e. Brownian movement (Nb) and thermophoresis (Nt) separately. There is a strong elevation in temperature with both parameters. Increasing values of Nb (Fig. 8) correspond to smaller diameter nanoparticles in the Buongiorno model. This results in greater ballistic collisions between the nanoparticles and an intensification in chaotic motions. The Brownian motion term, $+Nb \theta' \phi'$ is enhanced in Eqn. (9) and the regime is energized. Heat transfers are boosted as the boundary thermal thickness layer is encouraged, confirming the heat enhancement properties achieved with nanofluids. Fig. 9 also demonstrates that there is a noteworthy boost in the computed heat transfer with larger values of Nt . Thermophoretic body force $+Nt \theta'^2$ is enhanced in the energy Eqn. (9) with increment in thermophoresis parameter, Nt . The movement of nanoparticles under large temperature gradient is assisted with rising thermophoretic term. This also serves to elevate the thermal boundary layer viscosity on the Riga plate sensor.

Fig 10 shows the evolution in temperature with a change in Prandtl number. All profiles decay sharply from the Riga plate surface initially and then merge further in the free stream. As Prandtl number is increased, the heat conduction of the nanofluid is reduced. This inhibits heat diffusion in the regime and induces a cooling effect. Thermal boundary layer thickness is strongly suppressed. Prandtl number defines the momentum diffusivity relative to the heat diffusivity. For $Pr = 1$, both flow velocity and thermal diffusion occurs at the similar rate. For $Pr > 1$, momentum diffusion rate exceeds thermal diffusion rate. A considerable variation in

the temperature field is therefore attained with using a different base fluid and nanoparticles in the Riga sensor regime.

Fig 11 shows the impact of thermal generation (source) term, $Q = \frac{2Q_0L}{\rho C_p U_0 e^L x}$, on thermal transport profiles. The case of thermal absorption ($Q < 0$) is not considered. As anticipated, the heat source term, $+Q \theta$ is enhanced with greater values of Q . This initially produces a strong boost in temperatures near the Riga sensor plate surface (wall). However further from the wall there is a reverse in the effect and temperature is suppressed. The impact of heat source in the regime is therefore not consistent and is a function of the transverse location from the wall. Profiles are generally linear decays close to the wall but become increasingly parabolic with further distance from the wall.

Fig 12 displays the impact of thermal stratification term, St on the energy distributions. A marked decrement in temperature is observed with greater values of St . The regime is cooled and the thermal boundary layer thickness is depleted with more intense thermal stratification. Stronger thermal stratification effectively delays the thermal diffusion in the regime. Temperature is therefore a maximum when the thermal stratification effect is a minimum ($St = 0.1$). The implication is that if thermal stratification is neglected in the Riga plate transport model, temperatures are *over-predicted*. Inclusion of thermal stratification therefore allows a more accurate appraisal of the heat transfer behaviour, as also confirmed in Hayat *et al.* [35].

Figs. 13- 17 illustrate the progress in nanoparticle species mixture $\phi(\eta)$ with diverse selected parameters. In Fig. 13 a significant reduction in nanoparticle concentration is observed with large Brownian movement term (Nb). At low values of Nb the concentration magnified near the plate (Riga plate surface) which is eliminated at higher values of Nb . As noted earlier, higher Nb values imply smaller diameter nanoparticles. The chaotic motion is increased in the regime. However the upsurge in ballistic collisions which produces heating, circumvents the diffusion of nanoparticles in the boundary layer. This damps the reacting species (nanoparticle) concentration magnitude and deplete the nanoparticle boundary layer thickness. Fig. 14 shows that increasing thermophoresis term (Nt) opposes the effect of Brownian motion (Nb). There is a strong accentuation in nanoparticle concentrations and species boundary layer thickness is elevated. While Nt and Nb both feature in the terms, $+Nb \theta' \phi'$ and $+Nt \theta'^2$ in the energy Eqn. (9), they are also coupled in the term, $+\frac{Nt}{Nb} \theta''$, in the concentration boundary constraints Eqn. (10). Both parameters then exert a direct influence on nanoparticle concentration

distribution. Fig. 15 depicts that with rising in solutal stratification term, Sm , there is a strong reduction in nanoparticle concentration values. The term, $-Sc Sm f'$ in Eqn. (10) is increased with greater Sm values and inhibits nanoparticle migration (diffusion). The solutal stratification parameter, Sm also features in the wall species boundary condition (11), viz $\phi(0) = 1 - Sm$. Higher Sm values therefore also reduce the nanoparticle concentration boundary layer thickness. Fig. 16 displays the elevation in the Schmidt number, Sc , a marked depletion in nanoparticle species, and this impact is emphasized close to the Riga plate sensor surface. Further from the wall the profiles merge and Schmidt number exerts a much weaker influence. Concentration boundary layer thickness is thereby depleted with rising Sc values. Schmidt number defines the relationship between the momentum diffusivity and the nanoparticle molecular diffusivity. For $Sc < 1$, the mass diffusivity overshoots the momentum diffusivity and vice versa for $Sc > 1$. For $Sc = 1$ both diffusivity rates are equal, also the velocity (hydrodynamic) and nanoparticle concentration boundary layer thickness are of equal magnitude. Clearly with $Sc > 1$ the nanoparticle mass diffusion is inhibited. The nature of the nanoparticles selected for deployment in the Riga plate sensor system is therefore critical in determining the mass diffusion behaviour in the magnetic nanofluid. Fig. 17 displays the concentration distribution in the regime for different values of reacting species term (δ). The homogenous destructive chemical mixture of order-one is modelled in Eqn. (10) with the term, $-2Sc \delta \phi$. Since the chemical reaction is *destructive*, more nanoparticles are converted to another species. The original nanoparticle species concentration magnitudes are therefore reduced as observed. Nanoparticle concentration boundary layer thickness is decreased with large chemical reaction effect. The non-reactive case is retrieved for $\delta = 0$. With increasing δ values, the concentration peak near the Riga plate sensor wall is also progressively displaced closer to the wall and the concentration overshoot is also suppressed.

Table 2 documents the variation in skin friction $C_f Re_x^{1/2}$, heat gradient number $Nu_x Re_x^{-1/2}$ and mass gradient number $Sh_x Re_x^{-1/2}$ with all key terms. An increment in Riga magnetization parameter (H) elevates the wall drag force and temperature gradient number while the species gradient number is reduced. With enhancing Grashof number (Gr), wall friction and Nusselt number are also boosted, meanwhile Sherwood number is reduced. Increasing radiative parameter (Rd) weakly enhances skin friction but strongly boosts the Nusselt and Sherwood numbers, indicating higher heat distribution and nanoparticles mass transfer to the wall (Riga plate surface). A boost in the Brownian movement term (Nb) damps the wall skin friction, strongly decreases the Nusselt number and significantly amplifies the Sherwood number (mass

transfer gradient at the wall). Rising thermophoresis term (Nt) weakly increases skin friction, weakly reduces the Nusselt number and very substantially suppresses the Sherwood number (since nanoparticle mass transfer is raised in the region, the transit of nanoparticles to the wall is strongly reduced). An elevation in Prandtl number (Pr) reduces skin friction, noticeably boosts the Nusselt number (thermal gradient at the wall) - since nanofluid temperature is *reduced*- and very markedly depletes the Sherwood number. A boost in thermal source term ($Q > 0$), reduces skin friction and increases Nusselt number, although it induces a significant fall in Sherwood number magnitudes. A boost in mass transfer gradient (Sc) weakly increases the wall friction and weakly enhances the Nusselt number, but strongly elevates Sherwood number (since nanoparticle concentrations *in the boundary layer* are diminished and net migration of nanoparticles to the wall is therefore boosted). With more intense chemical reaction (δ), a slight rise in the wall skin friction and temperature gradient (Nusselt number) is noticed, but a significant enhancement in the species gradient (Sherwood number) is obtained. With increasing thermal stratification parameter (St), both wall skin friction and nanoparticle concentration gradient (Sherwood number) are weakly reduced, whereas thermal gradient at the wall (Nusselt number) number is strongly enhanced. With increasing mass (solutal) stratification parameter (Sm), there is no tangible modification in skin friction, whereas there is a slight rise in Nusselt number and a prominent decrease in Sherwood number.

6. Concluding Remarks

A theoretical study has been presented for convective chemically reacting flow of a magnetized Buongiorno nanofluid along an exponential stretchy Riga electromagnetic plate sensor with dual (thermal and solutal) stratification effects. The additional impacts of thermal sink/source and radiative heat flux are included. A computational solution of the transmuted non-dimensional ordinary differential boundary layer conservation equations with associated boundary constraints has been obtained with the second order finite difference Keller Box technique. Corroboration with earlier investigations were carried out. The key findings of the current study may be crystallized as follows:

- With enhancing magnetization term (H), velocity is elevated whereas temperature is suppressed.
- Increasing Grashof number (Gr) enhances velocity strongly near the sensor surface region and also decreases temperature throughout the boundary layer regime.

- Increasing thermophoresis term (Nt), radiative flux term (Rd), Brownian movement term (Nb), and thermal generation term (Q), all elevate the heat propagation, while it is decreased with higher values of Prandtl number (Pr) and thermal stratification term (St).
- Nanoparticle species reaction is significantly decreased for rising values of nanoparticle solutal stratification (Sm), Brownian motion parameter (Nb), Schmidt number and chemical reaction term (δ), meanwhile it is enhanced with thermophoresis parameter (Nt).
- Augmenting magnetization term (H) also elevates the wall drag force and thermal gradient (Nusselt number) but diminishes the species gradient at the wall (Sherwood number).
- With increasing chemical reaction (δ), a slight rise in the wall skin friction and Nusselt number is seen and a prominent upsurge in the Sherwood number is computed.
- With increasing thermal stratification parameter (St), both skin friction and Sherwood number are slightly decreased, but Nusselt number is considerably elevated.
- With increasing mass (solutal) stratification parameter (Sm), there is no significant change in wall in skin friction, whereas there is a slight enhancement in Nusselt number and a substantial depletion in Sherwood number.

The present study has shown that the Keller box finite difference technique is a very efficient method for computing electromagnetic actuator boundary layer flows. Future studies may generalize further the present analysis to consider *non-Newtonian* magnetic nanofluids which are also relevant to hybrid Riga plate electromagnetic devices.

Acknowledgements

The authors are grateful to all the reviewers for a number of their comments which have served to improve the article.

References

- [1] I. Nkurikiyimfura, Y. Wang, Z. Pan. Heat transfer enhancement by magnetic nanofluids-A review, *Renewable and Sustainable Energy Reviews*. 21 (2013) 548-561.
- [2] S. Doganay, A. Turgut, L. Cetin. Magnetic field dependent thermal conductivity measurements of magnetic nanofluids by 3ω method, *J. Magn. Mater.* 474 (2019) 199-206.
- [3] M.M. Bhatti, S.M. Sait, R. Ellahi. Magnetic nanoparticles for drug delivery through tapered stenosed artery with blood based non-Newtonian fluid, *Pharmaceuticals*. 15(11) (2022) 1352. <https://doi.org/10.3390/ph15111352>.

- [4] M.M. Rashidi, I. Mahariq, M.A. Nazari, Q. Accouche, M.M. Bhatti, Comprehensive review on exergy analysis of shell and tube heat exchangers, *J. Therm. Anal. Calorim.* 147 (2022) 12301-12311.
- [5] H.K. Hamzah, F.H. Ali, M. Hatami, D. Jing, M.Y. Jabbar. Magnetic nanofluid behaviour including an immersed rotating conductive cylinder: finite element analysis, *Scientific Reports.* 11 (2021) 4463. <https://doi.org/10.1038/s41598-021-83944-0>
- [6] H. Shafqat, S.E. Ahmed, T. Akbar. Entropy generation analysis in MHD mixed convection of hybrid nanofluid in an open cavity with a horizontal channel containing an adiabatic obstacle, *Int. J. Heat Mass Transf.* 114 (2017) 1054–1066.
- [7] A.S. Dogonchi, F. Selimefendigil, D.D. Ganji. Magneto-hydrodynamic natural convection of CuO-water nanofluid in complex shaped enclosure considering various nanoparticle shapes, *Int. J. Numer. Methods Heat Fluid Flow.* 29 (2019) 1663–1679.
- [8] F.A. Alwawi, H.T. Alkasasbeh, A.M. Rashad, R. Idris. MHD natural convection of Sodium Alginate Casson nanofluid over a solid sphere, *Results Phys.* 16 (2020) 102818. <https://doi.org/10.1016/j.rinp.2019.102818>
- [9] M.M. Bhatti, I.A. Sara. Bio-inspired peristaltic propulsion of hybrid nanofluid flow with Tantalum (Ta) and Gold (Au) nanoparticles under magnetic effects, *Waves in Random and Complex Media.* (2021). <https://doi.org/10.1080/17455030.2021.1998728>
- [10] Z. Ahmed, S. Nadeem, S. Saleem, R. Ellahi. Numerical study of unsteady flow and heat transfer CNT-based MHD nanofluid with variable viscosity over a permeable shrinking surface, *Int. J. Numer Methods Heat Fluid Flow.* 29 (2019) 4607-4623.
- [11] M. Hassan, A. Zeeshan, A. Majeed, R. Ellahi. Particles shape effects on ferrofluids flow and heat transfer under influence of low oscillating magnetic field, *J. Magn. Magn. Mat.* 443 (2017) 36-44.
- [12] M. Sheikholeslami, D.D. Ganji, M.Y. Javed, R. Ellahi. Effect of thermal radiation on magnetohydrodynamics nanofluid flow and heat transfer by means of two-phase model, *J. Magn. Magn. Mat.* 374 (2015) 36-43.
- [13] L. Gloag, M. Mehdipour, D. Chen, R.D. Tilley, J.J. Gooding, Advances in the application of magnetic nanoparticles for sensing, *Adv. Mat.* 31 (48) (2019) 1904385. <https://doi.org/10.1002/adma.201904385>
- [14] I. Koh, L. Josephson, Magnetic nanoparticle sensors, *Sensors.* 9(10) (2009) 8130–8145.
- [15] V.V. Avilov, Electric and magnetic fields for the Riga plate, Technical Report, FRZ Rossendorf (1998).

- [16] T. Salahuddin, M.Y. Malik, A. Hussain, S. Bilal, M. Awais, I. Khan. MHD squeezed flow of Carreau-Yasuda fluid over a sensor surface. *Alex. Eng. J.* 56 (2017) 27–34.
- [17] A. Shafiq, Z. Hammouch, A. Turab, Impact of radiation in a stagnation point flow of Walters' B fluid towards a Riga plate, *Therm. Sci. Eng. Prog.* 6 (2018) 27-33.
- [18] A. Ahmad, S. Asghar, S. Afzal, Flow of nanofluid past a Riga plate, *J. Magn. Magn. Mat.* 402 (2016) 44-48.
- [19] T. Hayat, M. Khan, M.I. Khan, A. Alsaedi, M. Ayub, Electro magneto squeezing rotational flow of Carbon (Cu)-Water (H₂O) kerosene oil nanofluid past a Riga plate: a numerical study, *PLoS One.* 12 (8) (2017) e0180976.
<https://doi.org/10.1371/journal.pone.0180976>
- [20] M. Ayub, T. Abbas, M.M. Bhatti, Inspiration of slip effects on electro magnetohydrodynamics (EMHD) nanofluid flow through a horizontal Riga plate, *Euro. Phys. J. Plus.* 131 (2016) 1-9.
- [21] A. Anjum, N.A. Mir, M. Farooq, M. Javed, S. Ahmad, M.Y. Malik, A.S. Alshomrani, Physical aspects of heat generation/absorption in the second-grade fluid flow due to Riga plate: application of Cattaneo-Christov approach, *Results Phys.* 9 (2018) 955-960.
- [22] R. Ellahi. The effect of MHD and temperature dependent viscosity on the flow of non-Newtonian nanofluid in a pipe: Analytical solution, *Applied Math Mod* 37(3) (2013) 1451-1467.
- [23] R. Ellahi, A. Zeeshan, F. Hussain, T. Abbas. Thermally charged MHD Bi-phase flow coatings with non-Newtonian nanofluid and Hafnium particles along slippery walls, *Coatings.* 9(5) (2019) 300. <https://doi.org/10.3390/coatings9050300>
- [24] R. Ellahi, S.M. Sait, N. Shehzad, Z. Ayaz. A hybrid investigation on numerical and analytical solutions of electro-magnetohydrodynamics flow of nanofluid through porous media with entropy generation, *Int J Numerical Method Heat and Fluid Flow* 30(2) (2020) 834-854.
- [25] M.A. Teamah, W.M. El-Maghlany, Augmentation of natural convective heat transfer in square cavity by utilizing nanofluids in the presence of magnetic field and uniform heat generation/absorption, *Int. J. Therm. Sci.* 58 (2012) 130-142.
- [26] C. Zhang, L. Zheng, X. Zhang, G. Chen. MHD flow and radiation heat transfer of nanofluids in porous media with variable surface heat flux and chemical reaction, *Appl. Math. Mod.* 39(1) (2015) 165-181.
- [27] I. Ahmad, A. Abbasi, W. Farooq, M. Ahmad. Chemically reacting flow water-and kerosene-Based nanofluid in a porous channel with stretching walls, *J. Nanosci. Nanotech.* 11(2) (2020) 169-194.

- [28] M. Farooq, A. Anjum, T. Hayat, A. Alsaedi, Melting heat transfer in the flow over a variable thickness Riga plate with homogeneous-heterogeneous reactions, *J. Mol. Liq.* 224 (2016) 1341-1347.
- [29] S.O. Salawu, A.M. Obalalu, M.D. Shamshuddin, Nonlinear solar thermal radiation efficiency and energy optimization for magnetized hybrid-Prandtl -Eyring nanoliquid in Aircraft, *Arab. J. Sci. Eng.* (2022). <https://doi.org/10.1007/s13369-022-07080-1>
- [30] M. Ramzan, M. Bilal, J.D. Chung, Radiative Williamson nanofluid flow over a convectively heated Riga plate with chemical reaction-A numerical approach, *Chin. J. Phys.* 55(4) (2017) 1663-1673.
- [31] Teresa A.P. Rocha-Santos, Sensors and biosensors based on magnetic nanoparticles, *TrAC Trends in Analyt. Chem.* 62 (2014) 28-36.
- [32] J.M. Perez, L. Josephson, R. Weissleder. Use of magnetic nanoparticles as nano-sensors to probe for molecular interactions, *Chem Biochem.* 5 (2004) 261–264.
- [33] M.Z.H. Supian, N.A.A.M. Nasir, A. Ishak, Stagnation point flow and heat transfer over an exponentially stretching/shrinking Riga plate with effects of radiation and heat source/sink, *Magnetohydrodynamics*, 57(3) (2021) 405-416.
- [34] N.S. Yusof, S.K. Soid, M.R. Illias, A.K.A. Aziz, N.A.A.M. Nasir, Radiative boundary layer flow of Casson fluid over an exponentially permeable slippery Riga plate with viscous dissipation, *J. Adv. Res. Appl. Sci. Eng. Tech.* 21 (2020) 41-51.
- [35] T. Hayat, M. Rashid, M. Imtiaz, A. Alsaedi, MHD effects on a thermo-solutal stratified nanofluid flow on an exponentially radiating stretching sheet, *J. Appl. Mech. Tech. Phys.* 58(2) (2017) 214-223.
- [36] V.S. Patil, Md. Shamshuddin, K. Ramesh, G.R. Rajput, Slipperation of thermal and flow speed impacts on natural convective two-phase nanofluid model across Riga surface: Computational scrutinization, *Int. Commun. Heat Mass Transf.* 135 (2022) 106135. <https://doi.org/10.1016/j.icheatmasstransfer.2022.106135>.
- [37] H. B. Keller, A new difference scheme for parabolic problems, In: Hubbard, B., Ed., *Numerical Solutions of Partial Differential Equations.* 2 (1971) 327-350.
- [38] H. T. Basha, R. Sivaraj, V. R. Prasad, O. Anwar Bég, Computation of non-similar flow of a magnetic pseudoplastic nanofluid over a circular cylinder with variable thermophysical properties and radiative flux, *Int. J. Num. Meth. Heat Fluid Flow.* 31(5) (2020)1475-1519.
- [39] G. Kumaran, R. Sivaraj, V.R. Prasad, O. Anwar Bég, R.P. Sharma, Finite difference computation of free magneto-convective Powell-Eyring nanofluid flow over a permeable

cylinder with variable thermal conductivity, *Physica Scripta*, 96 (2021) 025222.
<https://doi.org/10.1088/1402-4896/abd121>

[40] G. Kumaran, R Sivaraj, V.R. Prasad, O. Anwar Bég, Numerical study of axisymmetric magneto-gyrotactic bioconvection in non-Fourier tangent hyperbolic nano-functional reactive coating flow of a cylindrical body in porous media, *Euro. Phys. J. Plus*. 136 (2021) 1107.
<https://doi.org/10.1140/epjp/s13360-021-02099-z>

[41] H.T. Basha, R. Sivaraj, V. R. Prasad, O. Anwar Bég, Entropy generation of tangent hyperbolic nanofluid flow over a circular cylinder in the presence of nonlinear Boussinesq approximation: A non-similar solution, *J. Therm. Anal. Calorim.* 143 (2021) 2273–2289.

[42] M.A. Qureshi, Thermal capability and entropy optimization for Prandtl-Eyring hybrid nanofluid flow in solar aircraft implementation, *Alex. Eng. J.* 61(7) (2022) 5295-5307.

[43] W.F. Hughes and F. J. Young, *The Electro magneto dynamics of Fluids*, Wiley, New York (1966).